In-situ TEM investigation of toughening in Silicon at small scales

Inas Issa [1,*], Christoph Gammer [2,†], Stefan Kolitsch [2,3,†], Anton Hohenwarter [1], Peter J. Imrich [1,4], Reinhard Pippan [2], Daniel Kiener [1,*]

[1] Department Materials Science, Chair of Materials Physics, Montanuniversität Leoben, Jahnstrasse 12, A-8700, Austria
[2] Erich Schmid Institute of Materials Science, Austrian Academy of Sciences, Jahnstrasse 12, A-8700 Leoben, Austria
[3] Materials Center Leoben Forschung GmbH, Roseggerstrasse 12, A-8700 Leoben, Austria
[4] Infineon Technologies Austria AG, Siemensstrasse 2, A-9500 Villach, Austria

We report a length-scale-controlled Brittle-Ductile Transition giving rise to significant toughening of a commonly brittle material. Using quantitative *in-situ* Transmission Electron Microscopy (TEM) fracture experiments at room temperature on single crystal Silicon, we find that large samples fracture concordant with the brittle bulk behavior at a stress intensity $K_{IC} \sim 1$ MPa.m$^{1/2}$. Below characteristic dimensions of about 250 nm, however, the fracture toughness strikingly increases inversely with size to at least triple. As evidenced from advanced *in-situ* TEM nanoscale strain mapping the stresses at the crack tip approach the theoretical strength. At the same time, below this critical transition length nucleation and propagation of dislocations was observed, shielding the crack tip and enabling the unprecedented rise in fracture toughness. These first time *in-situ* TEM observations in nanoscale Silicon at room temperature open new strategies to simultaneously strengthen and toughen indispensable yet brittle functional materials solely by geometrical miniaturization.

Keywords: Size scale effect; Fracture toughness; Brittle Ductile Transition (BDT); Single crystal (SC) Silicon (Si); In-situ TEM; Nanoscale fracture experiments; Toughening

Introduction

Highly brittle materials such as Si, GaAs, etc., commonly experience brittle fracture before noticeable dislocation plasticity at room temperature (RT), owed to high Peierls stresses of their crystal lattice. However, size effects giving rise to higher material strengths in the submicron-scale [1–12] may impact the brittle ductile transition (BDT) and toughening when characteristic dimensions become small enough, even for highly brittle materials. Fundamentally, reaching sufficiently high stresses to nucleate and move dislocations from an atomistic stress concentrator prior to fracture would generate a shielding effect, decreasing the local stresses at the crack tip [13]. This enables toughening of brittle materials, a feature predominantly observed for metals.

Si, the most abundant functional material in modern technological devices, is known to be almost ideal brittle. The BDT Temperature (BDTT) of macroscopic Si is 562 °C at 1.3×10^{-6} s^{-1} strain rate. This can be higher or slightly lower depending on different experimental conditions, in particular the strain rate [14–17]. Shifting the BDTT to RT solely by geometric reduction and thus toughening the material at ambient conditions would be a key enabler for improving performance of future microelectronics devices.

Notably, the RT elastic strain limit of 100 nm pristine Si nanowires reaches $10-16\%$ [18], approaching the theoretical elastic limit ($\sim 17-20\%$) [19], with ~ 20 GPa estimated fracture stress,

* Corresponding authors.
E-mail addresses: Issa, I. (inas.issa@unileoben.ac.at), Kiener, D. (daniel.kiener@unileoben.ac.at).
† These authors contributed equally to this work.

1369-7021/© 2021 The Author(s). Published by Elsevier Ltd. https://doi.org/10.1016/j.mattod.2021.03.009This is an open access article under the CC BY license (http://creativecommons.org/licenses/by/4.0/).

while Molecular Dynamics (MD) simulations reported dislocation emission from a surface step at 13.2% strain at 300 K in pristine Si tensile specimens [20].

Literature reported BDT and increase of the fracture toughness (K_{IC}) of Si nanopillars [21,22] and nanoparticles [23] at RT, in compression tests. However, compression presents an extrinsic effect and mechanical constraint due to the confinement of featured cleavage planes between two anvils, inhibiting crack propagation when samples become small enough [24] and is therefore unsuited for studying BDT of highly brittle materials. Moreover, literature on small scale Si fracture experiments mostly concern the microscale [25,26], where a BDT is only observed at high temperatures (HT). Jaya et al. [26] relate the change in fracture mechanism at 300 °C, well below the BDTT of bulk Si [14–16,24–29], to a size effect in their 2 µm samples. Unfortunately, no clear scale effect on BDT can be extracted since thermal energy is vital in nucleating/activating dislocations at reduced stresses. Moreover, five times smaller specimens (~ 450 nm thick) tested at RT [30], demonstrated the opposite behavior with purely brittle fracture. Thus, a change in fracture behavior and ductility in Si at small scales is only reported at high temperature in microspecimens [25,26,31].

Our hypothesis is that the size effect enabling reaching the ideal tensile strength in Si for small enough defect-free volumes may have a profound and so far unexplored impact on the fracture resistance, characterized by K_{IC} and the related BDT, of one of the best mechanically characterized technical materials in the world. This would become exceedingly dominant at even smaller dimensions in the range of ~100 nm. Validation requires experiments at even smaller sizes than those tested by Gallo et al. [30] and confirmation of presumed fracture mechanical conditions.

Knowledge concerning the possibility to shift the BDTT to RT solely by geometric reduction to the sub-micron scale is still lacking, however, of vital importance for damage tolerance in the framework of ongoing miniaturization trends of components. To close this gap, we explore the size range [90 – 350] nm via quantitative *in-situ* TEM fracture experiments on pristine pre-notched single crystal (SC) Si bending beams in conjunction with advanced *in-situ* nanoscale strain mapping [32] and detailed Finite Element Method (FEM) simulations.

Materials and methods

Sample fabrication using FIB

(100) Si wafers provided from Infineon Technologies Austria AG (Villach, Austria), and (110) Si wafers from CrysTec GmbH (Berlin, Germany), both of high purity (undoped, resistance > 1000 Ωcm) and grown by the Czochralski method, are used in this study as starting materials.

A single cantilever bending test geometry is chosen, with the beams clamped on one side, see SI-Fig. 1(a) and (b) in SI-1, to reflect the most common fracture experiment geometry used at small scales [26,30]. This was proven to be the most tolerant for misalignment problems between the indenter tip and the sample surface. The free end avoids residual stresses that could be imposed in double clamped bending beams, while the rectangular shape allows a straight forward analysis of K_{IC} using Linear Elastic Fracture Mechanics (LEFM). Furthermore, in application MEMS components (e.g. actors or sensors) are typically loaded in bending. The bending beams, fabricated using Focus Ion Beam (FIB) milling from (100) Si wafers, are oriented along [011] direction and notched along (011)[100] schematically shown in SI-Fig. 1(b) and (c) in SI-1 and revealed by the corresponding diffraction pattern (DP) presented as inset of SI-Fig. 1(c) in SI-1. The second set of bending beams FIB fabricated from (110) Si wafers are designed such that bending beams are oriented along [001] direction and notches along (001)[110]. For both sets, notches (cracks) are introduced in the <110> propagation direction. Notch orientation nomenclature: (plane)[front], where (plane) is the cleavage plane the crack is introduced for and the [front] direction is the direction normal to the projected plane (in TEM images, i.e. zone axis).

Samples are first shaped to a wedge by grinding and polishing. Subsequently, lamellas spanning over few 100 µm length and 20 µm in thickness are fabricated in the top surface of the wedge-shaped sample by a femtosecond laser system [35]. Further machining of the bending beams is carried out using a FIB LEO 1540XB (Zeiss, Oberkochen, Germany) operating at 30 kV. Coarse milling is performed with a milling current of 2 nA. A lower milling current is used for shaping the bending beams and final cuts are performed using 10 pA to remove redeposited layers. The beams aspect ratio is chosen to be roughly $\sim 1 \cdot 1 \cdot 5$ or $1 \cdot 2 \cdot 10$ ($T \cdot W \cdot L$), T for thickness, W for width and L for length. For dimension reference see inset in Fig. 1(a) and SI-Fig. 1(b) in SI-1, except for the thickness which is in the transmission direction. This choice of aspect ratio allows to mimic a standard configuration of a fracture experiment on pre-notched samples, where the length is large enough compared to thickness and width. This also prevents shear stress components especially at the fixed side of the beam when loading it downwards from the top side, as $\frac{L}{W} \geq 4$ is obtained [36]. All tested specimen dimensions are presented in SI-Table1 in SI-2.

Due to the importance of the thickness dimension in such size effect studies, analytic Electron Energy Loss Spectroscopy (EELS) is used for accurate thickness measurements [37]. Uncertainty for the thickness measurements using EELS is of few nm to ~20 nm with increasing sample thickness.

Sharp notches introduced with the electron beam in TEM

In the Cs corrected TEM JEOL 2100F operating at 200 kV, at high magnification (600 K), we focus the electron beam to cut notches through the thickness of the specimen over a length a. These notches are very sharp with a radius equal to few atomic columns up to less than 2 nm maximum, see SI-Fig. 1(d) in SI-1, making them comparable to ideal sharp cracks. The notch length a is chosen to be in the range of $\sim\frac{W}{3}$, following works dedicated to the investigation of notch length and width ratio effects on the measured K_{IC}, ensuring a valid fracture experiment and a stable crack [25,38,39].

Structure recovery (recrystallisation of the FIB damaged layer)

Due to its potential effect on the measured mechanical parameters, the amorphous Si emerging as a damage layer during FIB fabrication [33] and obviously displayed in TEM images is recrystallized through annealing under high vacuum after FIB machining and notching. This is performed *in-situ* in the

Please cite this article in press as: I. Issa et al., Materials Today (2021), https://doi.org/10.1016/j.mattod.2021.03.009

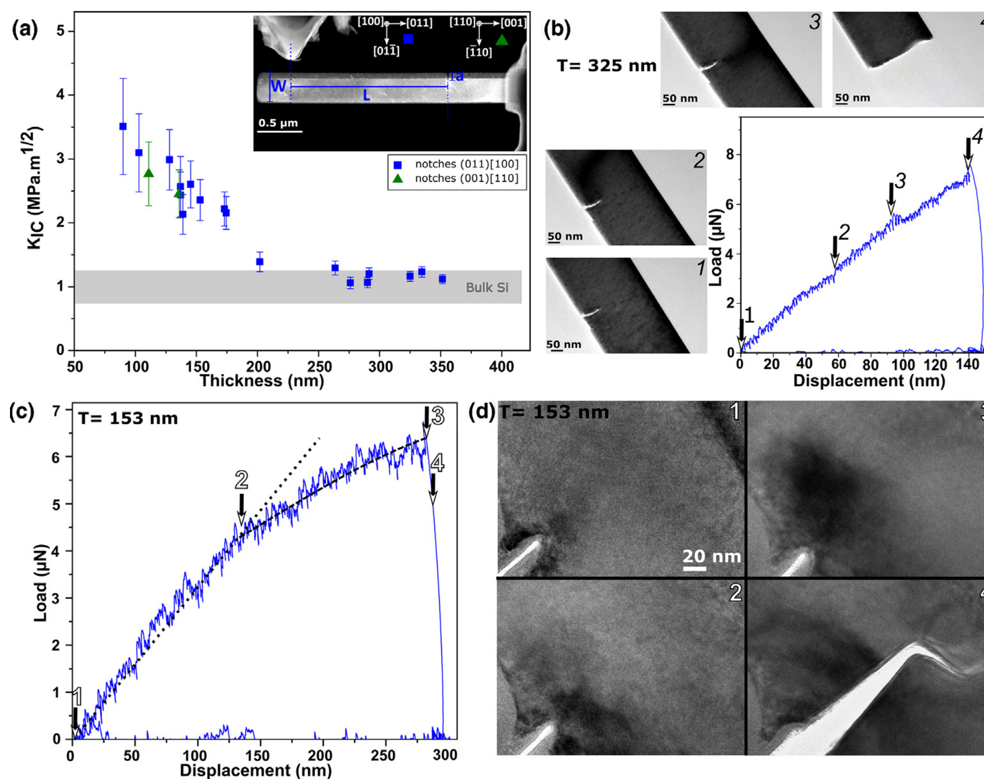

FIGURE 1

In-situ TEM experiments demonstrating size dependent fracture toughness in Si. (a) Fracture toughness K_{IC} versus thickness for 20 nanoscale specimens having two different crystallographic orientations. The grey band represents K_{IC} values for bulk Si [44], varying between $[0.7 - 1.3]$ $MPa.m^{1/2}$. Inset: STEM HAADF image of the experimental setup indicating geometrical dimensions length (L), width (W), and crack length (a). The thickness (T) is in the third dimension. All specimen dimensions and data are provided in **SI-2, Table 1**. (b) Load–displacement data of a 325 nm thick Si bending beam, insets: TEM images correlated to loading steps 1–4. The video test is provided as **SI-(*T* = 325 nm)**. (c) Load–displacement response of a 153 nm Si bending beam with extrapolation of linear elastic behavior (dotted line). (d) TEM images correlated to loading steps 1–4 in (c). The video test is provided as **SI-(*T* = 153 nm)**. Both samples were notched along $(011)[100]$ in the $\left[01\,\bar{1}\right]$ crack propagation direction.

TEM using a double tilt heating sample holder, model 652, tantalum® from GATAN, Inc. at roughly half of the Si melting temperature ($0.54{\cdot}T_m \sim 700$ °C) for 20 min. This annealing process in the TEM serves three purposes: recrystallisation of the damaged layer [34,40], annihilation of possible pre-existing dislocations [41], and removal of Ga implantation [40]. However, after annealing at 700 °C, few nm scale features are observed on the specimen surface. We regard that these are Ga droplets diffused out from the implanted specimen volume, also observed in [26], and some Si clusters from the recrystallized amorphous Si [40]. Latter work shows that elastic properties of FIB milled Si nanowires are recovered after annealing. Corresponding TEM investigations for recrystallisation of the outer layer and surface features proving diffusion of Ga from the implanted volume to the surface are presented in SI-3. Nevertheless, most important to note is that the notch (Crack) was not produced by FIB, but was generated by the electron beam. Hence the main part of the material in the vicinity of the crack tip is an FIB unaffected Si. Moreover, Weak Beam Dark Field (WBDF) TEM images confirming the dislocation free nature of the specimens and release of the elastic strain between the outer damage/recrystallized layer and the specimen volume after annealing are provided in SI-3.

In-situ TEM fracture experiments

The *in-situ* TEM fracture experiments are performed using a Hysitron Picoindenter PI-95 from Hysitron, Inc. running feedback loop enabled displacement-controlled experiments. A conductive wedge diamond tip from Synton MDP is used for bending the notched cantilevers. Tests are generally performed at displacement rates of 1 or 2 nm/s unless stated differently. This corresponds to strain rates of $2.15{\cdot}10^{-4}$ s^{-1} and $4.3{\cdot}10^{-4}$ s^{-1}, respectively, for a typical specimen with dimensions of $T = 128$ nm and $L = 1.6$ μm. The strain rate is calculated using: $\dot{\varepsilon} = \frac{3}{2}\cdot\left(\frac{W}{L^2}\right)\cdot\dot{\Delta v}$, where $\dot{\Delta v}$ is the displacement rate. Load-displacement data are collected with 200 points per second, and a synchronized video of the experiment is recorded with a frame duration of 33 ms and a pixel resolution of 1.28 nm. A typical *in-situ* TEM test is provided in **SI-Typical_Test (acc. X10)**. The videos tests of the two specimens presented in Fig. 1 are provided as **SI-(T = 325 nm)** (acc. X3) and **SI-(T = 153 nm) (acc. X6)**.

Data evaluation

LEFM is used to calculate the critical stress intensity at fracture K_{IC} using Eq. (1) [42]:

Please cite this article in press as: I. Issa et al., Materials Today (2021), https://doi.org/10.1016/j.mattod.2021.03.009

$$K_{IC} = \left(\frac{F \cdot L}{T \cdot W^{3/2}}\right) f\left(\frac{a}{w}\right) \quad (1)$$

Here F is the force at fracture, and $f(a/W)$ is a geometrical factor depending on the ratio $\frac{a}{W}$.

$f(a/W)$ is calculated for a single notch cantilever bending test as given by Eq. (2) [43]:

$$f\left(\frac{a}{W}\right) = 4\frac{\left\{(3\left(\frac{a}{W}\right)^{0,5}\left(1,23 - \left(\frac{a}{W}\right)\left(1-\frac{a}{W}\right)\right))\left(-6.09 + 13.96\left(\frac{a}{W}\right) - 14,05\left(\frac{a}{W}\right)^2\right)\right\}}{2\left(1+2\left(\frac{a}{W}\right)\right)\left(1-\frac{a}{W}\right)^{1,5}} \quad (2)$$

Error bars primarily account uncertainty on the length L, as due to the wedge tip radius the actual loading point can shift several nanometers, as well as the uncertainty on the thickness measured using EELS which can vary from a couple to few tens nm.

Details to the conducted FEM simulations as well as any other in-depth analysis are provided in the Supplementary Information.

Results

Size effect on K_{IC}

Fig. 1(a) presents the variation of K_{IC} with thickness (T), ranging from [90 – 350] nm. Eighteen specimens (blue symbols) are fabricated with zone axis [100], oriented along [011] and notched alongside $[01\bar{1}]$, also representing the loading direction, as detailed in SI-Fig. 1(b) in SI-1. Two specimens were designed with zone axis [110], oriented along [001] with notches alongside $[\bar{1}10]$ (green symbols).

In this specimen geometry, the critical dimension is $(W - a)$, with W being the width of the bending beams and a the initial pre-crack length. Since dimensional ratios of the specimens were kept about constant (see section Materials and Methods 2.1), for convenience and comparison to literature, data plots and related discussions relate to T. As shown in Fig. 1(a), for samples with $T > 250$ nm K_{IC} is in accordance with bulk Si data [44]. Strikingly, samples with $T \leq 250$ nm exhibit a steady increase of K_{IC} to at least three times higher values. Before going into details, assigning this increase of K_{IC} to a material size effect and elucidating possible origins, strict validation of the chosen linear elastic approach and the prevalence of *plane strain* loading conditions is compulsory to establish a foundation for the subsequent data analysis. This is presented in SI-2, where based on an analytical assessment of Irwin's plastic zone r_p as well as three-dimensional FEM simulations for decreasing T at constant W we validate the *plane strain* assumption. Within the tested size range possible influences due to the changing stress state are amounting to less than 5% (SI-Fig. 2b in SI-2).

Thus, the concepts of LEFM and the prevalence of *plane strain* conditions are applicable for our analysis. The well-known thickness or size effect on the fracture toughness of conventionally sized ductile samples in the transition from *plane strain* to *plane stress* does not influence the fracture resistance in the current work. Thus, we state that the striking increase of K_{IC} for $T \leq 250$ nm in Fig. 1(a) must have its origin in another length-scale related effect. This newly discovered size effect on fracture toughness at RT in notched Si nanobending beams represents an unknown intrinsic property of Si existing at very small length scales.

On the origin of the size effect on K_{IC}

WBDF TEM imaging confirms that specimens contain no dislocations, (SI-3). Furthermore, sharp notches, i.e. cracks, are of critical essence in fracture testing, and herein notches tip radii are from few atomic columns to 2 nm maximum (SI-Fig. 1(d) in SI-1). The FIB damage, such as amorphous surface layer and Gallium implantation, is removed after annealing *in-situ* in the TEM (high vacuum) (SI-3). Thus, the present specimens are pristine, in the range of 100 nm thickness, and with very sharp notches acting as crack tip singularities. Hence, due to the perfect crystallinity of the specimens, a high elastic strain and related extremely high stresses can be attained near the notch tip. Reaching the theoretical shear stress before the theoretical tensile stress [27,45], the material could overcome the activation energy barrier for dislocation emission and the Peierls stress to move dislocations. Once dislocations are emitted before reaching the fracture stress, they cause shielding to the crack tip, reducing the local crack tip stress intensity and give rise to a higher K_{IC}. The reality of this scenario is directly investigated via *in-situ* and postmortem TEM dislocation observations near the crack tip, as well as *in-situ* TEM strain mapping during the fracture test.

Dislocation observations and characterization

Evidently from the load–displacement data of the specimen with $T = 325$ nm in Fig. 1(b), the loading is entirely elastic until brittle fracture occurs at $K_{IC} = 1.16 \pm 0.08$ MPam$^{1/2}$. Correlated Bright Field (BF) TEM images matching different points along the curve show only a moving bending contour upon loading due to elastic changes in crystal orientation. The video test is provided as **SI-(T = 325 nm) (acc X3)**. Strikingly different, a linear fit to the force–displacement data for the specimen with $T = 153$ nm (dotted line in Fig. 1(c)), is possible from F = 0 to F = 4.31 μN (Point 2 in Fig. 1(c), and in agreement with accompanying FEM calculations. After this point a different function would be required to properly describe the data. Thus, the load–displacement data in Fig. 1(c) shows a slight deviation from linear elasticity at point 2, continuing until fracture. In the LEFM framework, as validated in SI-2, $K_{IC} = 2.37 \pm 0.32$ MPam$^{1/2}$. Correlated BF TEM images confirm that the linear elastic loading part until point 2 is devoid of any plastic activity. However, at point 2 and further, TEM images (2) & (3) in Fig. 1(d) illustrate, besides the bending contour, clear plastic activity in the notched zone. The specimen did not fracture completely, and the still connected beam bent back upon unloading. The video test is provided as **SI-(T = 153 nm) (acc X6).**

This specimen was thinned afterwards by FIB (5kV, 10 pA) for postmortem TEM observations.

Fig. 2**(a)** presents a BF TEM image (few degrees off from zone axis [100], using $\boldsymbol{g}(02\bar{2})$), revealing dislocation lines in front of the arrested crack tip. Based on the possible activated slip systems obeying the visibility criterion ($\boldsymbol{g}.\boldsymbol{b} \neq 0$), we identified five screw and two edge dislocations $1/2 < 110 > \{111\}$ near the crack tip that perfectly match two systems along (111) and $(11\bar{1})$ slip planes, shown schematically in Fig. 2(a). Details on the dislocation analysis are given in SI-7.

As stated before, this specimen failed at $K_{IC} = 2.37 \pm 0.32$ MPa.m$^{1/2}$. Assuming that the crack was

Please cite this article in press as: I. Issa et al., Materials Today (2021), https://doi.org/10.1016/j.mattod.2021.03.009

ARTICLE IN PRESS

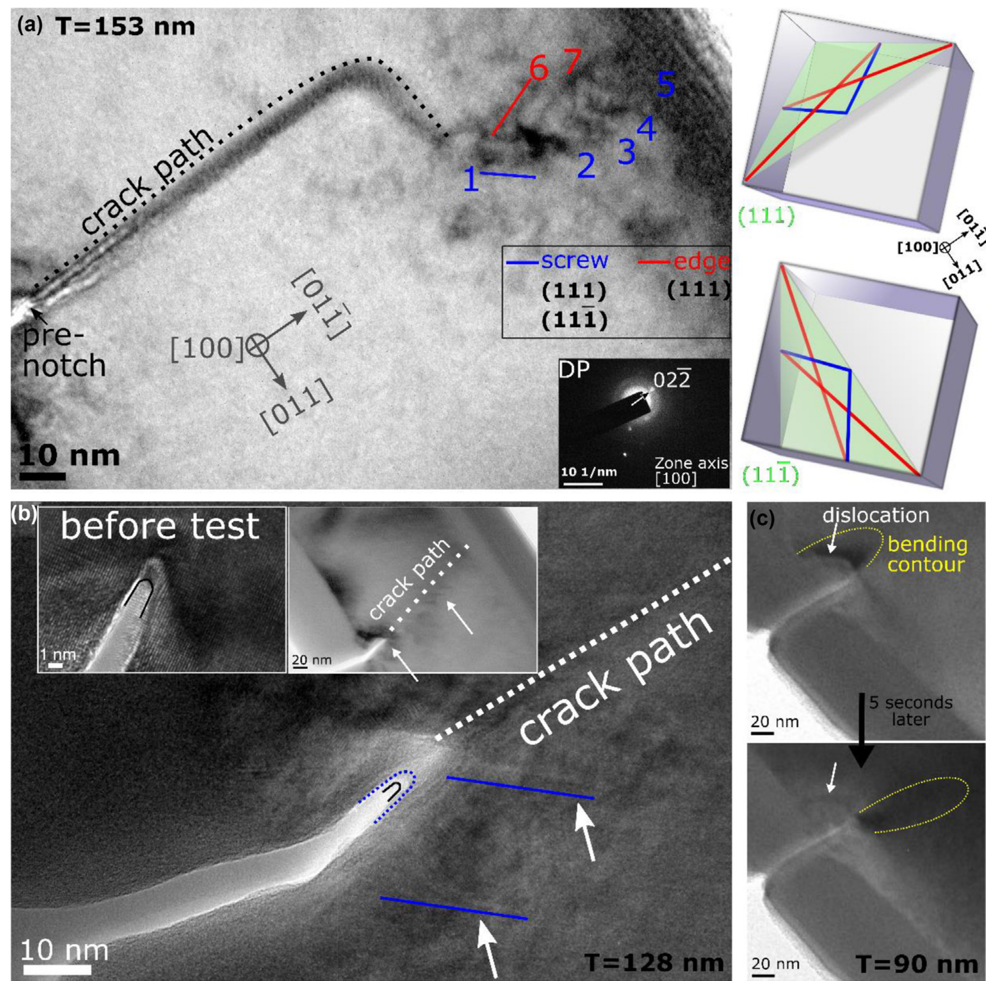

FIGURE 2

TEM observation of dislocation activity ahead of the crack tip. (a) FIB thinned post mortem BF TEM image of a crack tip trapped by few dislocations acquired under $g\left(02\bar{2}\right)$. Inset: corresponding diffraction pattern. Schematics depict possible screw (blue) and edge (red) dislocations on (111) and $\left(11\bar{1}\right)$ planes in Si for the given crystal orientaiton. (b) Post mortem HRTEM of a specimen with few dislocations revealed next to the crack path after one loading–unloading cycle and according stable crack propagation. Crack tip blunting is evident from the pre (black) and post testing (blue dotted) crack contour. (c) BF TEM images extracted from an *in-situ* test, showing a dislocation line and bend contour overlapping at the upper left side of the notch, which upon further loading become clearly resolvable, as the latter changes to the lower right side of the notch.

arrested/shielded by dislocations, we would expect a local shielding intensity $K_{D,exp} = (2.37 - 1.2) \cong 1.17$ MPa.m$^{1/2}$ when taking $K_{Griffith}$ of Si equal to 1.2 MPa.m$^{1/2}$ for convenience. Applying the simplified 2D back-stress model suggested by Higashida *et al*. [46]:

$$K_{D,cal} = \sum \left\{ \frac{3\mu b_i}{(1-v)(2\pi r_i)^{1/2}} cos(\varphi/2) sin(\varphi) \right\}$$

with μ (68 GPa) being the shear modulus, b (0.38 nm) the Burgers vector, v (0.28) the Poisson's ratio [47], r_i the distance of each dislocation to the first dislocation at the crack tip, and φ the angle between slip plane (111) and crack direction, taken to correspond to [011], we obtain $K_{D,cal} \sim 1.125$ MPa.m$^{1/2}$, convincingly close to $K_{D,exp}$ (1.17 MPa.m$^{1/2}$). Thus, we conclude that the observed dislocations suffice to explain the observed increase in K_{IC}.

To further corroborate dislocation activity, blunted crack tips after dislocation emission have been documented. A BF TEM image of a ~ 130 nm thick specimen shown in Fig. 2(b) reveals that the notch size became larger after crack propagation (blue dashed line) when compared to its initial size before testing (black line). Few dislocations along the crack path are observed, indicated by arrows in Fig. 2(b) and Fig. 2(b)-inset(right). Additionally, BF TEM images extracted from an *in-situ* test video in Fig. 2(c) show a curved dislocation line originating from the notch tip. Upon further loading, the bending contour becomes obviously discernable from this dislocation, as it changes position to the opposite side of the notch. These dislocation observations in the notch tip area are representative for specimens with thicknesses ≤ 250 nm and explain the increase of K_{IC}. 18 specimens tested in the current work have notches with <110> crack propagation direction on the {110} cleavage plane, thus along the easiest cleavage propagation direction and one of the favorable cleavage planes in Si predicted from ab-initio calculations [48,49]. Thus, despite examining this weakest crystallographic configuration prone to cleavage, the postmortem TEM image in Fig. 2(a) and the other *in-situ* TEM images presented in Fig. 2(b) and (c) show dislocations in small specimens.

Please cite this article in press as: I. Issa et al., Materials Today (2021), https://doi.org/10.1016/j.mattod.2021.03.009

We would expect this to be even more pronounced for non-cleavage orientations.

Approaching ideal strength in SI below ≤ 250 nm samples

In the notch tip singularity, the stress strongly increases proportional to $\frac{1}{\sqrt{r}}$, with *r* being the distance to the notch tip, as shown schematically in Fig. 3(b). To quantify this, we determined the local strain state via *in-situ* TEM strain mapping [32], see details in SI-4.

Fig. 3 shows the results for a notched bending beam with $T = 136$ nm in an area of 100 nm × 100 nm around the crack tip. The test is stopped during loading in the elastic regime, before plasticity or fracture would take place, and a strain map is acquired for the blue box in Fig. 3(a). The respective mapped area is shown in Fig. 3(b), while the resultant experimental elastic strain map in [001] direction around the notch is presented in the right hand side of Fig. 3(c).

This strain represents the tensile strain in the notch area (ε_{yy}), i.e. in the opening direction of the crack, which reaches ~8% at a distance of ~5 *nm* from the notch tip. For validation, the FEM elastic tensile strain map of a computational digital twin with identical dimensions loaded to the same point is displayed in Fig. 3(b)-(left-hand-side), demonstrating excellent agreement and validating the plane strain condition and respective data analysis.

Due to the crack tip singularity, the elastic strain can in fact reach even higher values than the measured 8%, as the strain map was acquired at a certain fixed displacement possibly close to the fracture load. Notably, due to slight thermal drift of the sample during strain mapping the force fluctuated by ~1 μN. Thus, potential deviations from linear elastic loading cannot be captured with certainty.

Based on the above analysis, the local strain at the crack tip can well approach the ~13% strain required for nucleation of a perfect half loop dislocation in the (111) shuffle set plane reported from MD simulations [20].

Taking the average instantaneous force F_i (4.1 μN) applied during strain mapping, we calculate the von Mises stress tensor, more details are presented in SI-5. At this loading stage, the Peierls stresses estimated as [4.6 – 5.77] GPa for Si [50] are easily

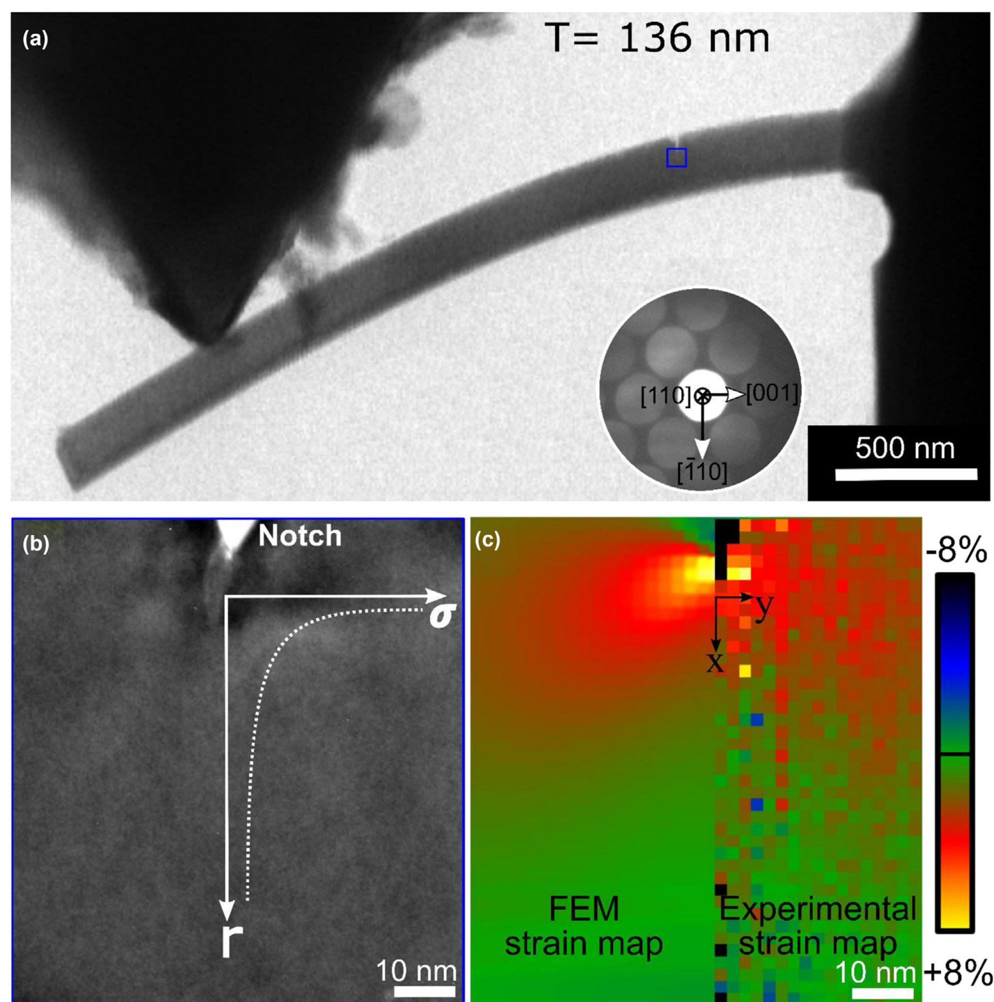

FIGURE 3

In-situ strain mapping during a nanoscale fracture experiment on single crystal Si. (a) STEM image of an *in-situ* test of a 136 nm thick specimen, stopped at an applied load of 4.1 µN for strain mapping of the notch area highlighted by the blue square. Inset: Reference DP acquired at zero load. (b) STEM image of the notch area for strain mapping and schematic of the tip singularity. (c) Right hand side: experimental strain map representing the strain along [001], i.e. in the opening direction of the crack (ε_{yy}). Left hand side: FEM strain distribution using a linear elastic model of identical dimensions and applied load.

Please cite this article in press as: I. Issa et al., Materials Today (2021), https://doi.org/10.1016/j.mattod.2021.03.009

overpassed in the tip singularity region of small specimens, as shown by the grey area in the von Mises stress map in SI-5. Thus, after dislocations nucleated, they can also propagate, as observed in Fig. 2.

Shear stress vs. normal stress acting in small and large bending specimens
To rationalize the change in material behavior from brittle to ductile for the present experiments by mere dimensional reduction, we follow the classical analysis [45,51] and compare the tensile and shear stress fields in front of the crack. Three-dimensional FEM simulations with constant ratios $T/W = 0.5$, $d/L = 0.3$, $L/W = 5$ and $a/W = 0.3$ were carried out for nine different thicknesses spanning from $T = 100$ to 2000 nm, respectively. The mesh in front of each specimens is equally designed by a spider shape, within a radius of $r = 50$ nm and a minimum element size of 0.5 nm. The load of the different specimen sizes is defined by a constant stress intensity $K = 1.2\ \mathrm{MPa}\sqrt{\mathrm{m}}$ [44].

In Fig. 4(a), the normal stresses in crack opening direction (σ_{YY}), lateral x-direction (σ_{XX}) and the equivalent Tresca shear stress (σ_{Tresca}) in the specimen center are plotted over the angle ϕ, where 0° denotes the crack growing path. Furthermore, the different line types represent four different T. The results are presented for a constant distance to the crack tip of $r = 2$ nm, where LEFM can still be applied to describe the stress and strain field, as confirmed in SI-Fig. 8 in SI 6.

Considering the stresses in the crack path direction at $\phi = 0°$, σ_{YY} decreases with decreasing T. Furthermore, the lateral stress σ_{XX} increases even more with increasing T. σ_{Tresca}, the important quantity for shear deformation, is higher for smaller T due to the different gradients of σ_{XX} for different T. This opposite trend in normal and shear stresses with reduced size eventually enables the nucleation of dislocations below a certain sample dimension.

Importantly, while the difference in σ_{Tresca} between specimens with the $T = 200$ nm and $T = 100$ nm is small but noticeably, for $T = 1000$ nm and $T = 2000$ nm the values are almost identical. Therefore, a saturation at common bulk levels occurs naturally for larger specimens. This is well represented by the increase in fracture toughness in Fig. 1(a), where a slight increase is seen for samples with $T \sim 250$ nm, and tremendous changes take place for $T < 250$ nm.

Importantly, this effect is not related to the bending geometry, but also uncovered for the tension loaded specimen, as presented in the SI-Fig. in SI-6.

Shift of BDTT of SI to RT at the nanoscale: Strain rate effect on $K_{\mathbf{IC}}$ at RT?
We revealed dislocation activity in front of a crack tip for specimens in the range ≤ 250 nm at RT, i.e. a BDT. Consequently, we expect also a strain rate sensitivity of K_{IC} in this size range. Fig. 5(a) presents six nominally identical specimens of $\sim$120 nm thicknesses tested using largely differing displacement rates $\Delta\dot{v}$, i.e. different strain rates $\dot{\varepsilon}$, calculated using: $\dot{\varepsilon} = \frac{3}{2} \cdot \left(\frac{W}{L^2}\right) \cdot \Delta\dot{v}$.

The specimens tested at high displacement rates of 10 and 100 nm/s result in a $K_{IC} \sim 1.3\ \mathrm{MPa.m^{1/2}}$, while those tested at lower strain rates of 1 and 2 nm/s exhibit higher K_{IC} by at least a factor of 2. Evidently, a strain rate effect on the K_{IC} of Si at small scales exists, even at RT. This is in line with our observation that the fracture process at such nanoscale dimensions is accompanied by dislocation activity, which is responsible for crack tip shielding and an according increase of K_{IC}. It also explains why a recent study by Sumigawa et al. [54] conducting fracture experiments on Si specimens in the range size of $[110 - 550]$ nm, did not observe a size effect on K_{IC}. Their tests were performed at rather high displacement rates of at least $[5 - 7]$ nm/s, corresponding to strain rates in the range $[0.0075 - 0.1]\ s^{-1}$, taking into account their geometry and dimensions as detailed in **SI-8**. In accordance with the present data in Fig. 5(a), no dislocation plasticity and consequently no toughening is expected in their experiments.

Discussion

All the tested specimens are pristine and self-similar. Nevertheless, a critical size ($T \sim 250$ nm) below which not only the strength, but also the toughness K_{IC} steadily increases is revealed from our study. This also confirms the single fracture test by Gerberich et al. on a 200 nm thick Si sample [53], suggesting a

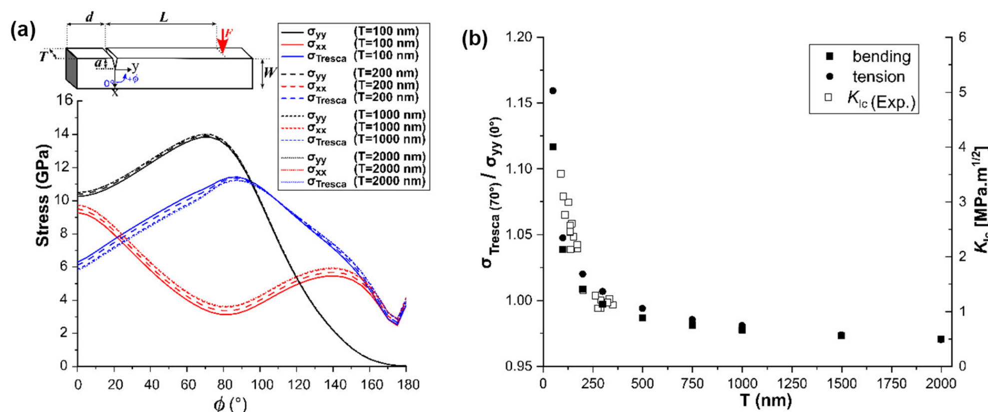

FIGURE 4

FEM calculations of the size dependent near tip stresses. (a) For the bending samples: Stress in *x*- (black lines) and *y*-direction (red lines) and the equivalent Tresca stress (blue lines) as a function of the angle ϕ for a distance of $r = 2$ nm to the crack tip and $K = 1.2\ \mathrm{MPa.m^{1/2}}$. The various line types denote different thicknesses T, while $T/W = 0.5$, $a/W = 0.25$, $L/W = 5$ and $d/L = 0.3$ were kept constant. (b) The ratio of the equivalent Tresca stress at 70° and the opening stress σ_{yy} (0°) (left Y axis, in bending and tension) and K_{IC} (right Y axis) are plotted over the specimen thicknesses.

Please cite this article in press as: I. Issa et al., Materials Today (2021), https://doi.org/10.1016/j.mattod.2021.03.009

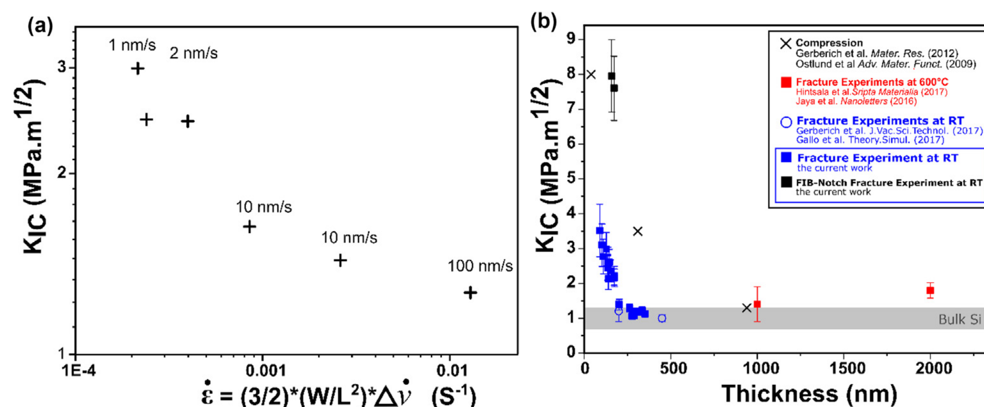

FIGURE 5

Strain rate and test setup effects on the fracture toughness of Silicon at small scales. (a) Strain rate effect on K_{IC} for specimens of ~120 nm thickness tested at RT. (b) Present size dependent K_{IC} data of Si (blue) compared to literature (compression at RT [21,52] and fracture experiments at HT [25,26] as well as RT [30,53]. Additionally, the extrinsic effect of large tip radii notches is demonstrated on two additional specimens having FIB introduced notches (black).

slight increase of K_{IC} at RT. Naturally the question for the fundamental origin of this length scale rises, and two general aspects have to be considered. First, the strength of the pristine specimens increases with reduced size [55–57], resulting in progressively higher endurable stress levels before fracture in ever smaller specimens, as evidenced via our *in-situ* strain mapping before fracture. Second, the shear stress level at the notch tip becomes eventually sufficient to nucleate dislocations before crack propagation, exerting local crack tip shielding [13] and rising the measured K_{IC} of small specimens.

To rationalize the observed critical dimension at which the intriguing ductilization of Si commences, from the three-dimensional FEM simulations presented in Fig. 4(a), we plot the significant stress ratio of the equivalent σ_{Tresca} at 70° to the opening stress σ_{YY} (0°), $(\frac{\sigma_{Tresca(70^\circ)}}{\sigma_{YY(0^\circ)}})$, over the calculated specimen thicknesses for all nine computed dimensions for tensile and bending loading in Fig. 4(b). This visualization relates to the initial idea of Kelly et al. [45], transferring the problem of cleavage or ductile fracture to the question whether the cleavage strength or shear strength is reached first upon loading. The data clearly shows an increase of $(\frac{\sigma_{Tresca(70^\circ)}}{\sigma_{YY(0^\circ)}})$, with decreasing specimens thicknesses, meaning the shear stress becomes larger than the opening stress component at the same external load. In comparison, thick samples suggest a saturation or only a slight variation of this ratio for larger samples being < 1. For specimens smaller than 250 nm a strong increase of the stress ratio sets in, allowing dislocation emission before cleavage fracture [51]. This increase in stress ratio has similar trending to the measured K_{IC} shown on the right-hand *y*-axis in Fig. 4(b).

In summary, reaching stresses approaching the theoretical strength at the crack tip in small specimens prior to fracture, as confirmed by in situ strain mapping, allows nucleation and propagation of dislocations. Moreover, as detailed by the three-dimensional FEM simulations, in close proximity of 2 nm to the crack tip, the ratio of $(\frac{\sigma_{Tresca(70^\circ)}}{\sigma_{YY(0^\circ)}})$ increases inversely with specimen size and becomes larger than 1 for specimens below 250 nm dimension. Hence, the critical shear stress to generate the dislocation in the small specimens at few nanometers around the crack tip becomes larger than the theoretical stress to cleave the Si. As mentioned before, this can then be seen as the case of a ductile fracture process, where the shear strength is reached before the cleavage strength upon loading.

This difference in $(\frac{\sigma_{Tresca(70^\circ)}}{\sigma_{YY(0^\circ)}})$ of small and large specimens in the critical regime of few nm is mainly caused by the deviation of the near tip stress field of small and large samples. For long cracks in linear elastic materials and very small values of (r/a), it is known that σ_{xx} equals σ_{yy}. However, for nano cracks even for distances of few nanometers a significant deviation can be observed when using the exact stress field solution. The deviation from the equivalence of σ_{xx} and σ_{yy} (SI-Fig. 8 in SI-6) in the near crack tip region causes an increase in σ_{Tresca} compared to σ_{yy}, facilitating plasticity over cleavage. Importantly, not only does the ratio $(\frac{\sigma_{Tresca(70^\circ)}}{\sigma_{yy(0^\circ)}})$ match the experimental toughening results, the FEM simulations also demonstrate that the behavior is comparable in tension (Fig. 4(b)), thus rendering this finding universal and not loading mode dependent.

Conclusion

In conclusion, the BDTT of Si is shifted to RT at the nanoscale. Compared to compression [21,52] and HT fracture experiments [25,26] that involve extrinsic effects and potentially overestimate K_{IC} of Si at small scales as presented in Fig. 5(b), this work reports for the first time a length scale dependent BDT and concurrent toughening of SC Si at RT. The fundamental concept is conceived as universal, as it only depends on elastic material properties and is not dependent on the loading mode (SI-Fig. in SI-6). As such, simultaneous strengthening and toughening of brittle SC materials by mere dimensional reduction should serve as a general strategy, opening new possibilities for damage tolerance in future micro- or nanomechanical systems or photonics applications [58].

CRediT authorship contribution statement

Inas Issa: Investigation, Methodology, Formal analysis, Conceptualization, Writing - original draft. **Christoph Gammer:** Investigation, Writing - review & editing. **Stefan Kolitsch:**

Please cite this article in press as: I. Issa et al., Materials Today (2021), https://doi.org/10.1016/j.mattod.2021.03.009

ARTICLE IN PRESS

Formal analysis, Methodology, Writing - review & editing. **Anton Hohenwarter:** Formal analysis, Writing - review & editing. **Peter J. Imrich:** Investigation, Writing - review & editing. **Reinhard Pippan:** Writing - review & editing. **Daniel Kiener:** Supervision, Conceptualization, Formal analysis, Writing - review & editing.

Declaration of Competing Interest

The authors declare that they have no known competing financial interests or personal relationships that could have appeared to influence the work reported in this paper.

Acknowledgements

I.I. and D.K. acknowledge funding by the European Research Council under Grant number 771146 (TOUGHIT). Authors would like to acknowledge Gabriele Felber and Herwig Felber for preparing wedge shaped samples, and Manuel Pfeifenberger and Alexander Jelinek for micro lamellas cut on the top surface of the wedge-shaped samples by a femtosecond laser. The authors gratefully acknowledge the financial support under the scope of the COMET program within the K2 Center "Integrated Computational Material, Process and Product Engineering, IC-MPPE" (Strategic Project P1.3).

Appendix A. Supplementary data

Supplementary data to this article can be found online at https://doi.org/10.1016/j.mattod.2021.03.009.

References

[1] M.D. Uchic, Science 305 (2004) 986–989.
[2] J.R. Greer, J.T.M. De Hosson, Prog. Mater. Sci. 56 (2011) 654–724.
[3] E. Calvié et al., Mater. Lett. 119 (2014) 107–110.
[4] S. Hoffmann et al., Nano Lett. 6 (2006) 622–625.
[5] J.R. Greer, W.D. Nix, Phys. Rev. B Condens. Matter Mater. Phys. 73 (2006) 1–6.
[6] C.A. Volkert, E.T. Lilleodden, Philos. Mag. 86 (2006) 5567–5579.
[7] D. Kiener et al., Adv. Eng. Mater. 8 (2006) 1119–1125.
[8] S. Lee et al., Nat. Commun. 5 (2014) 3033.
[9] L. Huang et al., Nat. Commun. 2 (2011) 547.
[10] Q. Sun et al., Scr. Mater. 65 (2011) 473–476.
[11] I. Issa et al., Acta Mater. 86 (2015) 295–304.
[12] S. Korte, W.J. Clegg, Philos. Mag. 91 (2011) 1150–1162.
[13] F. Cleri et al., Phys. Rev. Lett. 79 (1997) 1309–1312.
[14] C.S. John, Philos. Mag. 32 (1975) 1193–1212.
[15] S. Roberts, Proc. R. Soc. London. A. Math. Phys. Sci. 421 (1989) 25–53.
[16] P.D. Warren, Scripta Metall. 23 (1989) 637–642.
[17] J.R. Rice, G.E. Beltz, J. Mech. Phys. Solids 42 (1994) 333–360.
[18] H. Zhang et al., Sci. Adv. 2 (2016) e1501382.
[19] S.M.-M. Dubois et al., Phys. Rev. B 74 (2006) 235203, https://doi.org/10.1103/PhysRevB.74.235203.
[20] J. Godet et al., Phys. Status Solidi Appl. Mater. Sci. 206 (2009) 1885–1891.
[21] F. Östlund et al., Adv. Funct. Mater. 19 (2009) 2439–2444.
[22] M. Chen et al., Nat. Commun. 11 (2020) 1–10.
[23] J. Deneen Nowak et al., Philos. Mag. 87 (2007) 29–37, https://doi.org/10.1080/14786430600876585.
[24] K. Kendall, Nature 272 (1978) 710–711.
[25] E.D. Hintsala et al., Scr. Mater. 130 (2017) 78–82.
[26] B.N. Jaya et al., Nano Lett. (2016).
[27] J. Samuels, S.G. Roberts, Experiments 1–23 (1989).
[28] M. Brede, Acta Metall. Mater. 41 (1993) 211–228.
[29] K.J. Hsia, A.S. Argon, Mater. Sci. Eng. A 176 (1994) 111–119.
[30] P. Gallo et al., Adv. Theory Simul. 1700006 (2017) 1–9.
[31] E.D. Hintsala, W.W. Gerberich, Materialia 4 (2018) 175–181.
[32] C. Gammer et al., Appl. Phys. Lett. 109 (2016) 081906, https://doi.org/10.1063/1.4961683.
[33] C.M. Lauener et al., Mater. Des. (2018).
[34] Y. Wang et al., Appl. Phys. Lett. 081905 (2015) 1–5.
[35] M.J. Pfeifenberger et al., Mater. Des. 121 (2017) 109–118.
[36] B.N. Jaya, C. Kirchlechner, G. Dehm, J. Mater. Res. 30 (2015) 686–698.
[37] T. Malis, S.C. Cheng, R.F. Egerton, J. Electron Microsci. Technol. 8 (1988) 193–200.
[38] B.N. Jaya, V. Jayaram, Int. J. Fract. 188 (2014) 213–228.
[39] I. Bar-On, F.I. Baratta, K. Cho, J. Am. Ceram. Soc. 79 (1996) 2300–2308.
[40] T. Fujii et al., Sensors Mater. 31 (2019) 683–695.
[41] D. Kiener et al., Philos. Mag. 92 (2012) 3269–3289.
[42] K. Matoy et al., Thin Solid Films 518 (2009) 247–256.
[43] S. Wurster, C. Motz, R. Pippan, Philos. Mag. 92 (2012) 1803–1825.
[44] B. Wong, J. Electrochem. Soc. 134 (1987) 2254.
[45] A. Kelly, W.R. Tyson, A.H. Cottrell, Philos. Mag. J. Theor. Exp. Appl. Phys. 15 (1967) 567–586.
[46] K. Higashida et al., Mater. Sci. Eng.: A 483-484 (2008) 13–18.
[47] M.A. Hopcroft, W.D. Nix, T.W. Kenny, J. Microelectromech. Syst. 19 (2010) 229–238.
[48] A. George, G. Michot, Mater. Sci. Eng. A 164 (1993) 118–134.
[49] R. Pérez P. Gumbsch, Acta Materialia. 48 (2000) 4517–4530, https://doi.org/10.1016/S1359-6454(00)00238-X.
[50] Z. Li, N. Mathew, R.C. Picu, Comput. Mater. Sci. 77 (2013) 343–347.
[51] J.R. Rice, R. Thomson, Philos. Mag. 29 (1974) 73–97.
[52] W.W. Gerberich et al., J. Mater. Res. 27 (2012) 552–561.
[53] W. Gerberich et al., J. Vac. Sci. Technol. A Vacuum, Surfaces, Film 35 (2017) 060801.
[54] T. Sumigawa et al., ACS Nano 11 (2017) 6271–6276.
[55] S.S. Brenner, Science 128 (1958) 569–575, https://www.jstor.org/stable/1754714.
[56] G. Richter et al., Nano Lett. 9 (2009) 3048–3052.
[57] L.Y. Chen et al., Nat. Mater. 14 (2015) 707–713.
[58] F. Priolo et al., Nat. Nanotechnol. 9 (2014) 19–32.

Please cite this article in press as: I. Issa et al., Materials Today (2021), https://doi.org/10.1016/j.mattod.2021.03.009